2020

Role of Nanoscale Roughness in the Heat Transfer Characteristics of Thin Film Evaporation

H. Hu
Purdue University

J. A. Weibel
Purdue University, jaweibel@purdue.edu

S V. Garimella
University of Vermont, sureshg@purdue.edu

Hu, H.; Weibel, J. A.; and Garimella, S V., "Role of Nanoscale Roughness in the Heat Transfer Characteristics of Thin Film Evaporation" (2020). *CTRC Research Publications.* Paper 352.
http://dx.doi.org/10.1016/j.ijheatmasstransfer.2020.119306

Role of Nanoscale Roughness in the Heat Transfer Characteristics of Thin Film Evaporation

Han Hu[1], Justin A. Weibel[2], and Suresh V. Garimella[2,3]
School of Mechanical Engineering, Purdue University
585 Purdue Mall, West Lafayette, IN, 47907 USA

Abstract

Thin film evaporation yields high local heat fluxes that contributes significantly to the total heat transfer rate during various two-phase transport processes including pool boiling, flow boiling, and droplet evaporation, among others. Recent studies have shown a strong correlation between the roughness of a surface and its two-phase heat transfer characteristics, but the underlying role of nanoscale surface roughness in thin film evaporation is not fully understood. In the present work, a thin film evaporation model is developed that accounts for the role of the roughness-affected disjoining pressure and flow permeability in determining the film thickness profile and heat transfer rate. Nanoscale surface roughness leads to a flatter evaporating meniscus profile when the effect of disjoining pressure is more pronounced of the two and promotes evaporation, consistent with previous experimental observations. However, our results reveal that surface roughness may also inhibit evaporation and lead to a steeper evaporating meniscus profile when flow permeability has the more pronounced influence on thin film evaporation. It is important to identify the specific surface roughness characteristics that determine whether disjoining pressure or flow permeaiblity has the stronger influence. To this end, a parametric study is performed that analyzes thin film evaporation on V-grooved surfaces of different depths and pitches. While the heat transfer rate increases monotonically with groove depth, there exists an optimal groove pitch that leads to a maximized evaporation rate. Also, when the groove pitch is smaller than a critical value, surface roughness inhibits thin film evaporation.

Keywords: Thin film evaporation, nanoscale roughness, evaporating meniscus, disjoining pressure

---

[1] Currently with the University of Arkansas
[2] Corresponding author. E-mail: jaweibel@purdue.edu (J.A. Weibel), sureshg@purdue.edu (S.V. Garimella)
[3] Currently President, University of Vermont

1. Introduction

Two-phase heat transfer is widely encountered in thermal management of microelectronics [1], water desalination in solar stills [2], steam boiling and condensation in power plants [3], ultrafast vitrification for cell cryopreservation [4], and other applications. In various two-phase processes, evaporation from the extended meniscus close to the three-phase contact line (also known as thin film evaporation) has a major contribution to the total heat transfer [5]. Experimental studies have shown that nanoscale surface roughness affects the meniscus profile and heat transfer rate in thin film evaporation [6]. For larger structures, *e.g.*, hoodoo structures [7], micropillars [8], sintered mesh [9], sintered microparticles [10], and hierarchical structures [11], local roughness at the contact line also plays a role in determining heat transfer rate. In order to design surface structures that provide further heat transfer enhancement, it is of fundamental significance to understand the heat transfer characteristics of the evaporating meniscus on rough surfaces.

As shown in Figure 1a, the evaporating meniscus can be divided into three regions: the adsorbed film, the evaporating thin film, and the intrinsic meniscus. Driven by the temperature difference between the solid surface and the vapor, heat is transferred by conduction in the liquid film and evaporation across the liquid-vapor interface. The heat flux in the evaporating thin film region is very high due to the low thermal conduction resistance across the film. As a result of the long-range solid-liquid intermolecular forces, an excess pressure known as the disjoining pressure is required for liquid molecules to escape from the evaporating thin film. Disjoining pressure increases rapidly with decreasing film thickness and fully suppresses evaporation in the adsorbed film region. The absolute liquid pressure becomes smaller as disjoining pressure increases. The disjoining pressure and capillary pressure therefore simultaneously drive liquid flow from the intrinsic meniscus to the evaporating thin film region to maintain the evaporation rate. For thin film evaporation on rough surfaces, the disjoining pressure and the flow permeability are affected by surface roughness, which in turn influence the thickness profile and the heat transfer rate of the evaporating thin film.

Experimental studies have been performed to extensively characterize the thin film meniscus thickness profile and the heat transfer performance on planar surfaces. The thickness profile of the evaporating thin film can be directly measured using interferometry [6, 12-14] and reflectometry [14] techniques. On rough surfaces, Ojha *et al.* showed that increasing nanoscale surface roughness (RMS roughness of 1–12.5 nm) led to increased disjoining pressure, resulting in a flatter

evaporating meniscus and improved heat transfer performance [6]. However, quantitative correlations between surface roughness and thin film evaporation heat transfer characteristics are not yet available. A theoretical thin film evaporation model, which accounts for the effect of surface roughness, is required to develop such general correlations and design surface structures for improved thin film evaporation.

In seminal work modeling thin film evaporation, Potash and Wayner [15] derived the thickness profile and heat transfer rate of an evaporating meniscus based on the balance between evaporation and liquid flow driven by capillary and disjoining pressure. During the past several decades, this thin film evaporation model has been updated to account for slip boundaries [16], thermocapillary effects [16, 17], capillary suppression [5, 18], electrostatic disjoining pressure [17], thermal conduction [5, 17, 19, 20], partial wetting [21-23], and contact line motion [21-24]. None of these models accounts for the effect of surface roughness on disjoining pressure and flow permeability, which are key physical quantities that determine the heat transfer characteristics of thin film evaporation.

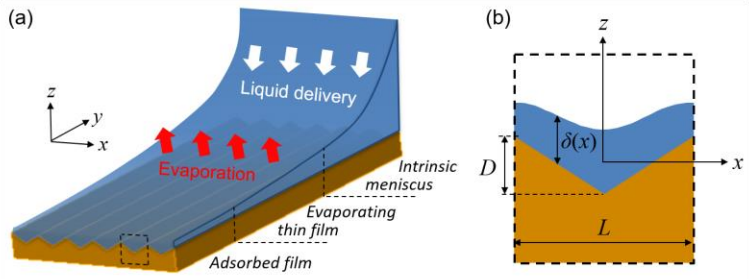

Figure 1. (a) Schematic drawing of thin film evaporation on a V-grooved surface. (b) Cross-sectional view of a zoomed-in section of the thin liquid film on the V-grooved surface characterized by depth D and pitch L.

Disjoining pressure plays a key role in driving liquid flow during thin film evaporation. The disjoining pressure model for an atomically smooth surface predicts that disjoining pressure, Π, scales with the inverse cube of the film thickness, δ, following, $\Pi = A/\left(6\pi\delta^3\right)$, where A is the Hamaker constant that characterizes the strength of the solid-liquid interactions [25, 26]. Even though experimental studies have identified inadequacies in this disjoining pressure model [27-

29] and proposed various empirical modifications [30, 31], this inverse cubic expression is still predominantly used in thin film evaporation models due to its simplicity. The use of an effective Hamaker constant [6, 32] is a simple empirical method for describing disjoining pressure on rough surfaces, which inherently assumes that surface roughness only affects the magnitude of the Hamaker constant, rather than affecting the disjoining pressure through a change in the inverse cubic relation with film thickness. However, there is no clear evidence supporting this approach for rough surfaces. Theoretical models for disjoining pressure on rough surfaces have been developed based on linear [33] and Derjaguin [33, 34] approximations, but the validity of these approximations across a range of different surface structures has not been demonstrated. Furthermore, the flow and pressure fields in the thin film are usually determined by solving the Poiseuille flow equation on planar surfaces, ignoring the effect of surface roughness. Through coarse-grained molecular dynamics simulations, Stukan *et al.* [35] demonstrated that nanoscale surface roughness may lead to a significant reduction in flow permeability. To accurately describe the heat transfer characteristics of thin film evaporation on rough surfaces, it is important to accurately represent the effects of surface roughness on disjoining pressure and flow permeability during thin film evaporation.

We develop a theoretical model for thin film evaporation that accounts for the effects of surface roughness on disjoining pressure and flow permeability. A V-grooved surface is investigated as a canonical rough surface geometry to validate the approach. The roughness-affected disjoining pressure is determined based on the Derjaguin approximation and validated against direct integration of the solid-liquid potential. The roughness-affected flow permeability is determined based on the balance between the driving pressure and the viscous resistance, and is validated against finite-volume simulations. The combined role of roughness-affected disjoining pressure and flow permeability in thin film evaporation is examined. A parametric study is performed to investigate the effect of the structure depth and pitch on the film thickness profile and the cumulative heat transfer rate.

2. Model development and discussion

2.1 Thin film evaporation on rough surfaces

In this section, a theoretical model is developed for thin film evaporation on rough surfaces. All symbols used in the model development equations are defined in the Supplementary Material.

Figure 1a shows a schematic drawing of an evaporating thin liquid film on a V-grooved surface and Figure 1b shows a cross-sectional view of a zoomed-in region of the thin film on the surface. The V-groove geometry is characterized by a depth, *D*, and a pitch, *L*. The following basic assumptions are used in this model:

i) The liquid film completely wets the rough surface.
ii) Van der Waals forces dominate the solid-liquid interactions.
iii) The effect of the surface roughness on thin film evaporation via changes in the liquid-vapor interfacial area and the conductance through the film is trivial (see Supplementary Material), and thus is not included in the model.
iv) One-dimensional conduction is assumed in the thin liquid film.

In the evaporating thin film, the liquid pressure, P_l, is related to the vapor pressure, P_v, according to the augmented Young-Laplace equation $P_v = P_l + P_c + \Pi_{rough}$, where Π_{rough} is the disjoining pressure on rough surfaces. The capillary pressure, P_c, is defined as $P_c = \gamma\kappa$, where γ is surface tension. The curvature, κ, is defined as $\kappa = \gamma\delta''\left(1+\delta'^2\right)^{-1.5}$, where δ' and δ'' are the 1st and 2nd order derivatives of the film thickness, δ, with respect to the *y*-axis (see Figure 1a), respectively.

Based on the continuity equation, the evaporating mass flux, j_m, can be determined with the gradient in liquid pressure following

$$\frac{dP_l}{dy} = \frac{\nu}{\delta K_{rough}} \int_{-\infty}^{y} j_m dy \tag{1}$$

where ν is the kinematic viscosity of the liquid. Substituting the expression of the liquid pressure, $P_l = P_v - P_c - \Pi_{rough}$, into Equation (1) gives

$$\frac{d}{dy}\left(\left[\frac{\gamma\delta'''}{\left(1+\delta'^2\right)^{1.5}} - \frac{3\sigma\delta'\delta''^2}{\left(1+\delta'^2\right)^{2.5}} + \frac{d\Pi_{rough}}{d\delta}\delta'\right]\frac{\delta K_{rough}}{\nu}\right) = -j_m \tag{2}$$

where δ''' is the 3rd order derivative of the film thickness with respect to the *y*-axis and K_{rough} is the flow permeability on the rough surface. The vapor pressure, P_v, vanishes during the substitution because it is not a function of the spatial coordinates. To solve this fourth order ODE, four boundary conditions are required. At $y = 0$, the film thickness is equal to the adsorbed film

thickness, δ_n. The gradient of the slope at $y = 0$ is zero, *viz.* $\delta'(0) = 0$ [5]. The far end boundary (at $y = L_y$) is given as $\kappa(L_y) = 1/R^*$, where R^* is the radius of curvature of the intrinsic meniscus. The fourth boundary condition is given by $\int_{-\infty}^{0} j_m dy = 0$ [5].

The evaporation mass flux can be calculated using Schrage's equation following [36]

$$j_m = \left(\frac{2\hat{\sigma}}{2-\hat{\sigma}}\right)\left(\frac{M}{2\pi R}\right)^{1/2}\left[\frac{P_{v,eq}(T_{lv})}{T_{lv}^{1/2}} - \frac{P_v(T_v)}{T_v^{1/2}}\right] \tag{3}$$

where $\hat{\sigma}$ is the accommodation coefficient of the liquid, M the molar mass of the liquid, R the universal gas constant, T_{lv} the liquid temperature at the liquid-vapor interface, T_v the vapor temperature, P_v the vapor pressure, and $P_{v,eq}$ the equilibrium vapor pressure at T_{lv}. Considering the effect of disjoining pressure and capillary pressure, the equilibrium vapor pressure deviates from the saturation vapor pressure following $P_{v,eq}(T_{lv}) = P_{sat}(T_{lv})\exp\left[\frac{P_{v,eq} - P_{sat} - (\Pi_{rough} + P_c)}{\rho_l T_{lv} R/M}\right]$ [37]. Assuming the vapor is not too far from the saturation state, $P_{v,eq}(T_{lv}) \approx P_{sat}(T_{lv})\exp\left[\frac{-(\Pi_{rough} + P_c)}{\rho_l T_{lv} R/M}\right]$. Based on the Clausius-Clapeyron equation, the saturation pressure at T_{lv} is $P_{sat}(T_{lv}) = P_v(T_v)\exp\left[\frac{Mh_{fg}}{R}\left(\frac{1}{T_v} - \frac{1}{T_{lv}}\right)\right]$. Therefore, the equilibrium vapor pressure at T_{lv} can be calculated as

$$P_{v,eq}(T_{lv}) = P_v(T_v)\exp\left[\frac{Mh_{fg}}{R}\left(\frac{1}{T_v} - \frac{1}{T_{lv}}\right) - \frac{(\Pi_{rough} + P_c)}{\rho_l T_{lv} R/M}\right] \tag{4}$$

Assuming one-dimensional conduction in the thin liquid film, the temperature of the solid surface, T_s, is related to the interfacial temperature, T_{lv}, following,

$$T_s - T_{lv} = \frac{\delta h_{fg} j_m}{k_l} \tag{5}$$

Substituting Equation (4) and Equation (5) into Equation (3), the interfacial temperature, T_{lv}, can be calculated using the following equation

$$\frac{k_{\mathrm{l}}\left(T_{\mathrm{s}}-T_{\mathrm{lv}}\right)}{\delta h_{\mathrm{fg}}}=\left(\frac{2\hat{\sigma}}{2-\hat{\sigma}}\right)\left(\frac{M}{2\pi R}\right)^{1/2}\left[\frac{P_{\mathrm{v}}}{T_{\mathrm{lv}}^{1/2}}\exp\left[\frac{Mh_{\mathrm{fg}}}{R}\left(\frac{1}{T_{\mathrm{v}}}-\frac{1}{T_{\mathrm{lv}}}\right)-\frac{\left(\Pi_{\mathrm{rough}}+P_{\mathrm{c}}\right)}{\rho_{\mathrm{l}}T_{\mathrm{s}}R/M}\right]-\frac{P_{\mathrm{v}}}{T_{\mathrm{v}}^{1/2}}\right] \tag{6}$$

Simultaneously solving Equation (2) and Equation (6) gives the thickness profile, $\delta=\delta\left(y\right)$, interfacial temperature profile, $T_{\mathrm{lv}}=T_{\mathrm{lv}}\left(y\right)$, and mass flux profile, $j_{\mathrm{m}}=j_{\mathrm{m}}\left(y\right)$, with known material properties (k_{l}, h_{fg}, M, ρ_{l}, $\hat{\sigma}$, γ, ν), operating conditions (T_{s}, T_{v}, and P_{v}), and structural characteristics of the rough surfaces.

In Equation (2) and Equation (6), the disjoining pressure, Π_{rough}, and the flow permeability, K_{rough}, of thin liquid films on rough surfaces are functions of film thickness and the surface structure. Separate models are developed to accurately predict Π_{rough} and K_{rough} on rough surfaces in the following Sections 2.2 and 2.3, respectively. The adsorbed film thickness, δ_{n}, is calculated by setting $j_{\mathrm{m}}=0$ in Equation (3). Equation (2) is solved using a shooting method with Newton's iteration, where the boundary value problem is converted to two initial value problems that are solved using the Runge-Kutta method. The details of the solution method can be found in the Supplementary Material.

2.2 Disjoining Pressure on Rough Surfaces

The disjoining pressure in a thin liquid film on a solid surface arises from the long-range intermolecular forces between the liquid and solid molecules. For a Lennard-Jones-type potential, the long-range interaction is given as $\Phi\left(r\right)=-\dfrac{A}{\pi^2\rho_{\mathrm{N,l}}\rho_{\mathrm{N,s}}}r^{-6}$, where r is the distance between the solid and liquid molecules, and $\rho_{\mathrm{N,l}}$ and $\rho_{\mathrm{N,s}}$ are the number densities of the liquid and solid molecules, respectively. By integrating the solid-liquid potential, the disjoining pressure profile of a thin liquid film is calculated as

$$\Pi_{\mathrm{rough}}^{\mathrm{int}}\left(x,y\right)=-\int_{-\infty}^{+\infty}\int_{-\infty}^{+\infty}\int_{\zeta\left(x,y\right)-\mathrm{Z}\left(x',y'\right)}^{+\infty}\rho_{\mathrm{N,l}}\rho_{\mathrm{N,s}}\Phi\left(x',y',z'\right)dz'dy'dx' \tag{7}$$

where $\zeta\left(x,y\right)$ is the liquid film profile and $\mathrm{Z}\left(x,y\right)$ is the solid surface profile. For a thin liquid film on a planar surface, the thickness profile, $\delta\left(x,y\right)=\zeta\left(x,y\right)-\mathrm{Z}\left(x,y\right)$, is uniform along the surface, $\delta\left(x,y\right)\equiv\delta$, and Equation (7) simplifies to the well-known disjoining pressure model for

planar surfaces, $\Pi = A/\left(6\pi\delta^3\right)$. While a simple expression for disjoining pressure is not always obtainable for rough surfaces, Equation (7) can be solved numerically to yield the exact solution of the disjoining pressure. However, it is inconvenient to lump the solution of the double integral into the thin film evaporation model. Alternatively, the Derjaguin approximation [38] has been widely used to calculate disjoining pressure on a non-flat surface [33, 39], where the local solid-liquid interaction of a curved surface can be approximated by that of a planar surface with the same local film thickness:

$$\Pi_{\text{rough}}^{\text{Derjaguin}}\left(x,y\right) = \frac{A}{6\pi\delta^3\left(x,y\right)} \tag{8}$$

Both Equation (7) and Equation (8) give the disjoining pressure profile in the *x*-*y* plane. For a thin liquid film on a two-dimensional structured surface with a known surface profile along the *x*-axis, $Z\left(x\right)$ ($\partial Z/\partial y = 0$), disjoining pressure only varies along the *x*-axis. As shown in Figure 1b, the coordinate system is set at the mean of $Z\left(x\right)$ to ensure $\int_{-L/2}^{-L/2} Z\left(x\right)dx = 0$. The mean film thickness along the *x*-axis is given as $\delta_0 = \frac{1}{L}\int_{-L/2}^{L/2}\delta\left(x\right)dx$. Because the thin film evaporation model developed in Section 2.1 is a two-dimensional model that only considers the flow (*y*) and thickness (*z*) directions, the mean disjoining pressure averaged along the *x*-axis, $\bar{\Pi}_{\text{rough}} = \frac{1}{L}\int_{-L/2}^{L/2}\Pi_{\text{rough}}\left(x\right)dx$, can be lumped into the thin film evaporation model to account for the solid surface profile variation along the *x*-axis.

In order to validate the simple expression for disjoining pressure in Equation (8), Figure 2a-b compares the Derjaguin approximation (Equation (8)) and the exact solution of the disjoining pressure obtained from the direct integration method (Equation (7)) for a thin liquid film (δ_0 = 10 nm) on a V-grooved surface with a depth of D = 5 nm and a pitch of (a) L = 100 nm and (b) L = 5 nm. A flat liquid film profile ($\zeta\left(x\right) \equiv \delta_0$) is used in the calculations. While the Derjaguin approximation accurately predicts the disjoining pressure profile for the rough surface with the large depth (L = 100 nm), it leads to an inaccurate prediction of the profile for the case with L = 5 nm. However, as shown in Figure 2c-d, the *mean* disjoining pressure is accurately predicted using the Derjaguin approximation for both L = 100 nm and L = 5 nm in a range of mean film thicknesses.

Therefore, we adopt the Derjaguin approximation to calculate the mean disjoining pressure in a thin liquid film on rough surfaces.

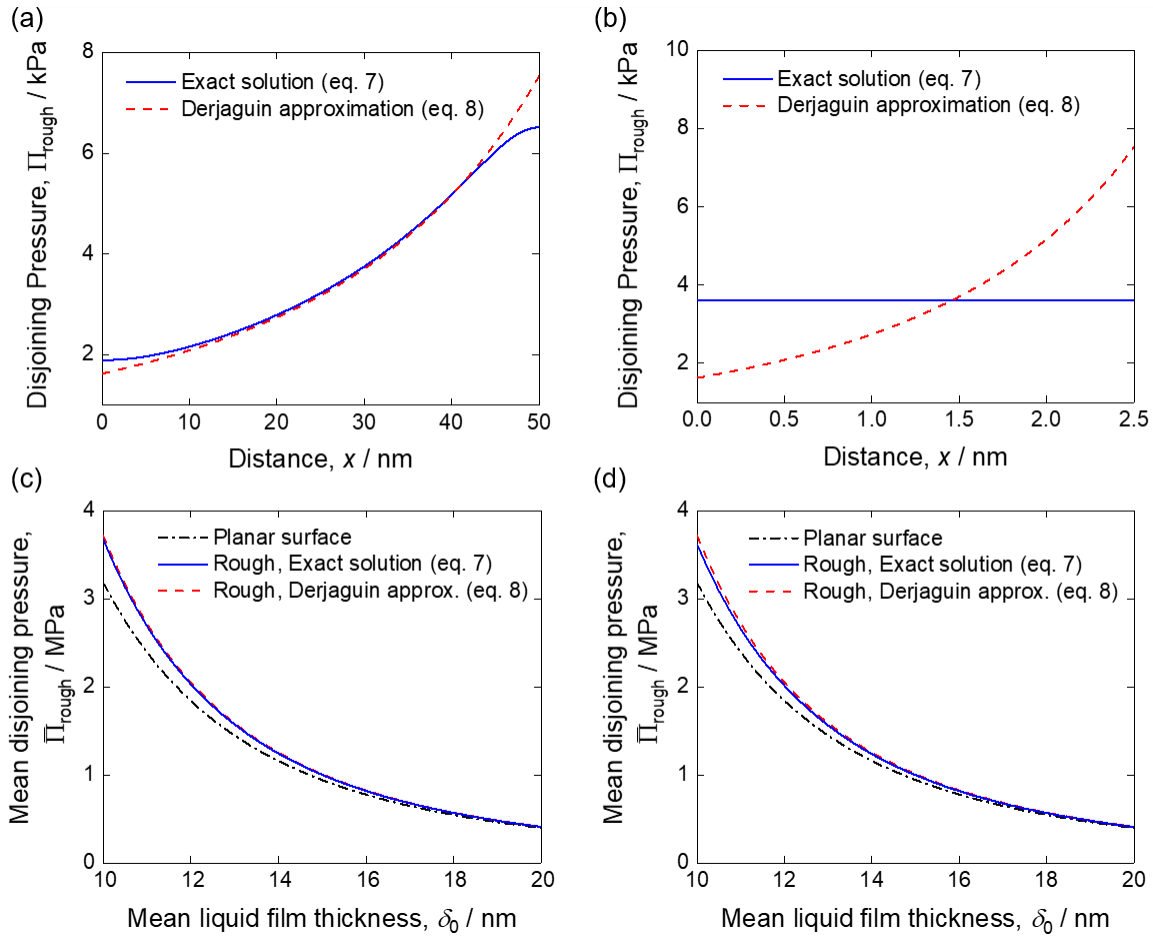

Figure 2. Validation of the Derjaguin approximation for the calculation of the disjoining pressure on a rough surface against the exact solution obtained from the integration of the solid-liquid potential: (a-b) disjoining pressure profile of a thin liquid film (δ_0 = 10 nm) on a V-grooved surface with a structure depth of D = 5 nm and a structure pitch of (a) L = 100 nm and (b) L = 5 nm; and (c-d) mean disjoining pressure as a function of mean liquid film thickness for D = 5 nm and (c) L = 100 nm and (d) L = 5 nm.

In the above calculations, the liquid film was assumed to have the flat profile, $\zeta(x) \equiv \delta_0$. Theoretical models have been developed to accurately predict the liquid film profile on rough surfaces by minimizing system free energy for both two-dimensional [34, 40] and three-

dimensional structures [41]. However, these models for liquid film profiles require the implicit solution of simultaneous integral equations, and therefore cannot readily be lumped into the thin film evaporation model. To obtain a simple expression for calculating disjoining pressure, a fitting equation is proposed based on the meniscus shape model developed in our previous study [41]. This fitting equation correlates the mean disjoining pressure with the relevant system parameters based on the models for liquid film profiles:

$$\bar{\Pi}_{\text{rough}} = \frac{A}{6\pi\delta_0^3}\left[1 + C\left(\frac{D}{\delta_0}\right)^2\left(\frac{2\pi\xi}{L}\right)^4\left(1+\left(\frac{2\pi\xi}{L}\right)^2\right)^{-2}\right] \tag{9}$$

where ξ is the healing length defined as $\xi = \delta_0^2 \Big/ \sqrt{A/(2\pi\gamma)}$ [33]. Based on the results calculated using the Derjaguin approximation (Equation (8)) and the theoretical model for liquid film profiles [41], the constant C is fitted to be 0.55 for the V-grooved surfaces.

Figure 3 compares the mean disjoining pressure model based on the Derjaguin approximation (Equation (8)) and the film-profile-based fitting (Equation (9)) for predicting disjoining pressure in thin liquid films on a planar surface and V-grooved surfaces with (a) different depths (D = 2.5 nm, 5 nm, and 7.5 nm) and a fixed pitch of L = 20 nm and (b) different pitches (L = 10 nm, 20 nm, and 30 nm) and a fixed depth of D = 5 nm. The solid lines represent the disjoining pressure model based on the Derjaguin approximation (Equation (8)), and the dashed lines represent the prediction of the film-profile-based fitting equation (Equation (9)). General agreement is observed between the film-profile-based fitting (Equation (9)) and the Derjaguin approximation (Equation (8)), where their deviation becomes more significant with increasing groove depth and decreasing groove pitch. For the remainder of this work, the film-profile-based fitting (Equation (9)) is used to predict the disjoining pressure in thin liquid films on rough surfaces, and is lumped into the thin film evaporation model developed in Section 2.1.

It is noted that in the log-log plot, the disjoining pressure model for the planar surface (black solid line) is a linear curve with a slope of -3, representing the inverse cubic relation. For rough surfaces, disjoining pressure is higher than that for a planar surface and increases with increasing groove depth or decreasing groove pitch. This effect is only pronounced in the region where the film thickness is comparable to the groove depth. When the film thickness is very small, a conformal film is expected, and the mean disjoining pressure can be accurately predicted using the model for a planar surface. On the other hand, when the film is very thick, the effect of surface

roughness on disjoining pressure is negligible, leading to a small deviation from the model for the planar surface. It is important to note that the trend in mean disjoining pressure on rough surfaces is not linear in the log-log plot, indicating that the disjoining pressure is not a simple power function of the film thickness. Therefore, the use of an effective Hamaker constant, which inherently assumes an inverse cubic relation, is not capable of accurately capturing the roughness-affected disjoining pressure behavior. It is noted that Equation (9) calculates the disjoining pressure based on a rough surface composed of multiple smooth sections that are joined together. As such, it is still limited by the framework of conventional disjoining pressure theory for planar surfaces [42] and its accuracy is expected to decrease for surfaces with very high aspect ratios. Nevertheless, the model developed here for disjoining pressure on rough surfaces offers a more robust description that will be useful in a broader range of physical processes including lubrication and convective-assembly.

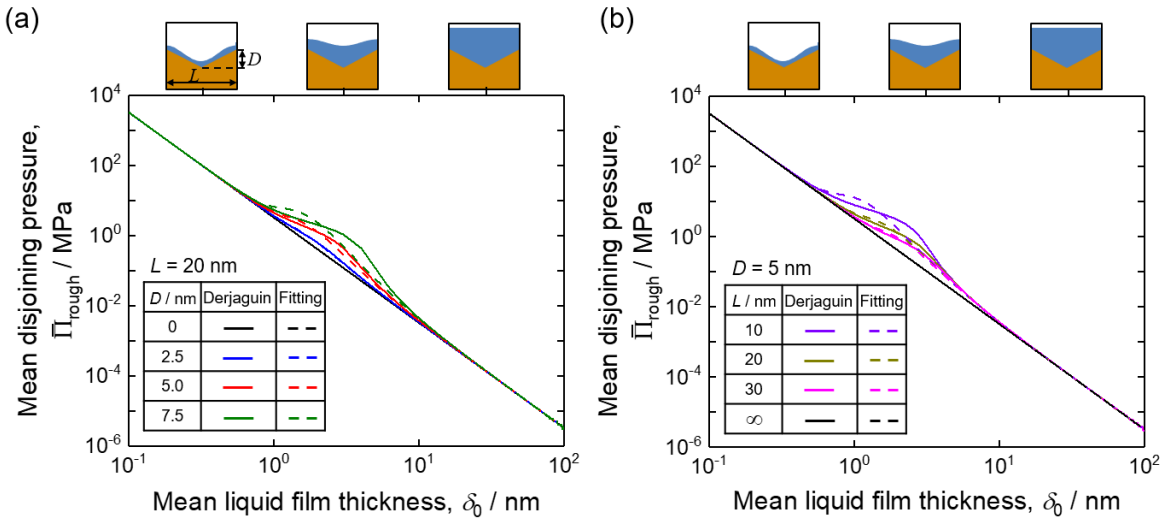

Figure 3. Prediction of the mean disjoining pressure in thin liquid films on V-grooved surfaces using the film-profile-based fitting equation (Equation (9)) and Derjaguin approximation (Equation (8)) for (a) different depths (D = 2.5 nm, 5 nm, and 7.5 nm) at a fixed pitch of L = 20 nm, and (b) different pitches (L = 10 nm, 20 nm, and 30 nm) at a fixed depth of D = 5 nm.

2.3 Flow Permeability on Rough Surfaces

Flow permeability is a parameter used to describe the viscous pressure drop in a liquid flowing through a medium, and is defined as $K = \rho_l \nu \bar{u} \big/ \left(\Delta P / L_y \right)$, where $\bar{u}$ is the superficial velocity, and

ΔP is the pressure drop across the length L_y. Based on a balance between the driving pressure and the viscous resistance,

$$\iint_{A_\mu} \tau_w dA = \iint_{A_p} \Delta P dA \tag{10}$$

where τ_w is the shear stress at the solid surface, A_μ the area on which the viscous resistance acts, and A_p the cross-sectional flow area. For liquid flow on a planar surface, assuming a parabolic velocity profile, the shear stress, $\tau_w = \mu\left(\partial u/\partial z\right)_w$, can be approximated as $\tau_w = 3\bar{u}/\delta$. Substituting the expression of the shear stress and flow permeability into Equation (10) gives $K_{planar} = \delta_0^2/3$, where δ_0 is the mean film thickness. For the V-grooved surface, as shown in Figure 4, the coordinate system is set with the z'-axis perpendicular to the liquid-vapor interface so that a parabolic velocity can be assumed as in the case of a planar surface. In the limiting case of a flat thin film (Figure 4a), the flow permeability is derived as (see derivation in the Supplementary Material)

$$\frac{K_{rough}}{K_{planar}} = \frac{1}{r} \tag{11}$$

where r is the Wenzel roughness ratio defined as the ratio of solid-liquid contact area to the footprint area. For a V-grooved surface, the Wenzel roughness ratio is $r = \sqrt{1+\left(2D/L\right)^2}$. In the case of a conformal thin film (Figure 4b), the flow permeability is derived as (see derivation in the Supplementary Material),

$$\frac{K_{rough}}{K_{planar}} = \frac{1}{r^2} \tag{12}$$

For any thin film profile between these extremes, the flow permeability falls between K_{planar}/r^2 and K_{planar}/r. In order to validate this flow permeability model, the prediction on V-grooved surfaces using Equation (11) and Equation (12) is compared with the exact solution obtained from the finite-volume numerical simulations (ANSYS Fluent) in Figure 4c. Good agreement is obtained between the simple permeability model and the exact solution, for both the flat thin film and the conformal thin film. During thin film evaporation, the film thickness typically ranges from several nanometers in the nonevaporating film to approximately 1 micron in the intrinsic meniscus. As a general rule, the thin film profile becomes approximately flat when the film thickness is

greater than half of the groove depth for a V-grooved surface [34]. Therefore, on V-grooved surfaces with depths on the order of 1-10 nm, a majority of the evaporating thin film will be relatively flat in shape along the *x*-axis (Figure 1). The flow permeability equation for the flat thin film, *viz.* Equation (11), is used for the rest of this work.

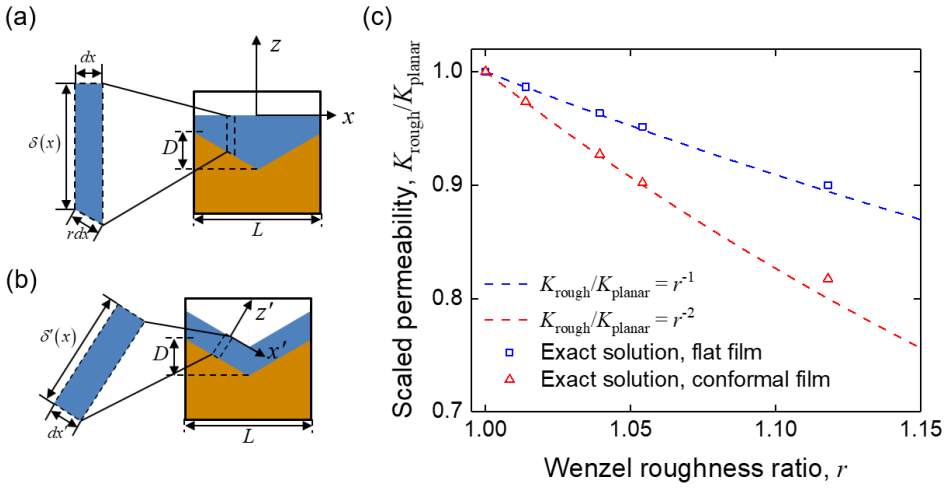

Figure 4. Effect of surface roughness on free-surface flow permeability in a liquid film: schematic diagrams of flow cross-sections on V-grooved surfaces for (a) a flat thin film and (b) a conformal thin film; and (c) comparison between the present flow permeability model for both the flat thin film (Equation (11)) and the conformal thin film (Equation (12)) and the exact solution for the permeability on V-grooves as a function of the Wenzel roughness ratio.

3. Results

3.1 Comparison with the Literature

The model is first compared with the literature to ensure that it recovers the known solution for predicting the thickness profile of an evaporating meniscus on a planar surface. Figure 5 compares the thickness profile predicted by the present model (solid lines) with Wang *et al.* [5] (dashed lines). For this comparison, the same liquid properties (octane) and operating conditions are input to the model as by Wang *et al.* [5], summarized in Table 1. The liquid surface tension and the kinematic viscosity at the operating condition (T_v = 343 K) are interpolated from Grigoryev *et al.* [43] and Harris *et al.* [44], respectively. Excellent agreement in the film thickness profile is obtained for four different intrinsic meniscus radii of curvature, *viz.* R^* = 0.2 μm, 0.4 μm, 2.5 μm, and 60 μm. The minor deviations between the predictions can be attributed to the numerical

implementation and possible mismatch in fluid properties that were not reported explicitly in Wang *et al.* [5].

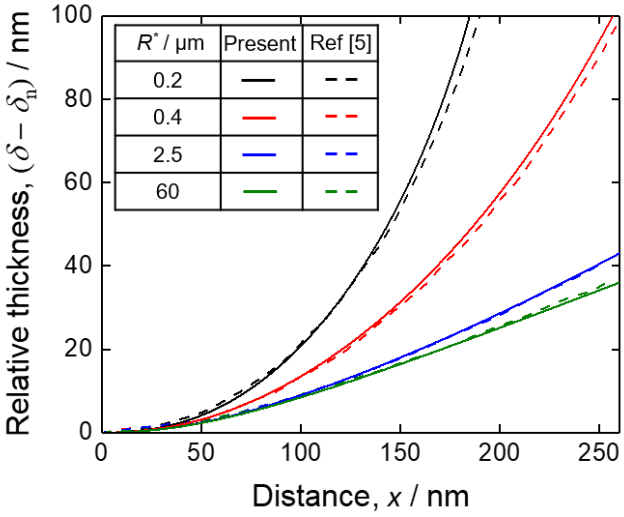

Figure 5. Comparison between the present work and Wang *et al.* 2007 [5] for the prediction of thickness profiles of thin liquid films on a planar surface with different intrinsic meniscus radii of curvature (R^* = 0.2 μm, 0.4 μm, 2.5 μm, and 60 μm).

Table 1. Material properties and operating conditions.

Property	**Value**	**Property**	**Value**
ρ_l (kg/m^3)	661.2 [5]	A (J)	6×10^{-20} [5]
k_l (W/mK)	0.11 [5]	M (kg/mol)	114.23×10^{-3}
h_{fg} (J/kg)	3.398×10^{5} [5]	P_v (Pa)	1.5828×10^{5} [5]
γ (J/m^2)	0.016 [43]	T_s (K)	344
$\hat{\sigma}$	1 [5]	T_v (K)	343
v (m^2/s)	4.806×10^{-7} [44]		

3.2 Roles of Roughness-affected Disjoining Pressure and Flow Permeability

In order to understand the roles of the roughness-affected disjoining pressure and flow permeability in thin film evaporation, the theoretical model is applied for thin liquid films evaporating on a planar surface and V-grooved surfaces with different groove depths and pitches.

The cumulative heat transfer rate as a function of film thickness is introduced to represent the heat transfer characteristics of thin film evaporation as

$$q(\delta) = \int_{C:\,\delta(y)} h_{fg} j_m d\delta \tag{13}$$

where h_{fg} is the enthalpy of vaporization of the liquid and j_m is the evaporative mass flux. The line integral represented by Equation (13) is calculated along the thickness profile of the evaporating meniscus, $\delta(y)$, from the non-evaporating film (where $\delta(0)=\delta_n$) .

Figure 6 shows (a) the thickness profile and (b) the cumulative heat transfer rate as a function of film thickness, for evaporating thin liquid films on a planar surface and a rough surface with D = 5 nm and L = 20 nm. The black and red solid lines represent the results for the planar surface and the rough surface with D = 5 nm and L = 20 nm, respectively. The evaporating meniscus on the rough surface is flatter (or more extended) than that on the planar surface, which is consistent with experimental trends observed in the literature [6]. It is shown in Figure 6b that the cumulative heat transfer rate on the rough surface with D = 5 nm and L = 20 nm is lower than that of the planar surface at relatively low film thicknesses (δ < 5 nm). This is due to the strong suppression of evaporation induced by the roughness-affected disjoining pressure. However, this suppression effect is only pronounced when the film thickness is very small (δ < 5 nm), and therefore does not significantly contribute to the cumulative heat transfer rate when considering the entire evaporating meniscus. For δ > 5 nm, because the evaporating meniscus is flatter on the rough surface, the cumulative heat transfer rate on the rough surface with D = 5 nm and L = 20 nm is higher than that on the planar surface.

In order to isolate the influence of the roughness-affected disjoining pressure, Π_{rough}, and the roughness-affected flow permeability, K_{rough}, the red dotted lines and the red dashed lines in Figure 6 represent the results accounting for only Π_{rough} and only K_{rough}, respectively. The results reveal the opposing influence of these two parameters. As discussed in Section 2.2, surface roughness leads to increased disjoining pressure, and therefore a stronger driving force for liquid delivery. As a result, when only Π_{rough} is considered, surface roughness leads to a flatter meniscus (Figure 6a) and higher cumulative heat transfer rate (Figure 6b). As discussed in Section 2.3, surface roughness leads to reduced flow permeability due to stronger viscous resistance. Therefore, when only K_{rough} is considered, surface roughness leads to a steeper meniscus (Figure 6a) and lower cumulative heat transfer rate (Figure 6b). For the specific case shown in Figure 6, the combined net influence makes the evaporating thin film flatter and the cumulative heat transfer

higher, indicating that disjoining pressure has a more pronounced influence than flow permeability on thin film evaporation for the rough surface with D = 5 nm and L = 20 nm.

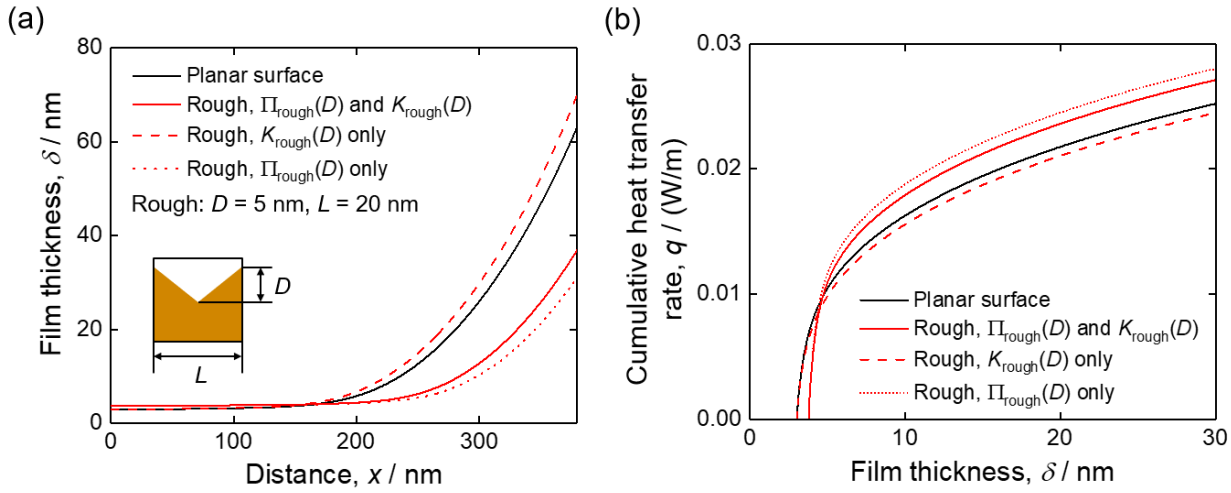

Figure 6. (a) The thickness profile and (b) the cumulative heat transfer rate as a function of film thickness for an evaporating meniscus on a planar surface and a rough surface (V-groove with D = 5 nm and L = 20 nm). The black solid lines represent the results for the planar surface. The red solid lines represent the results for the rough surface accounting for both the roughness-affected flow permeability, K_{rough}, and the roughness-affected disjoining pressure, Π_{rough}. The red dashed and dotted lines represent the results for the rough surface accounting for only K_{rough} and only Π_{rough}, respectively.

For different rough surfaces, it is also possible that K_{rough} has a more dominant influence on thin film evaporation. Figure 7 shows (a) the thickness profile and (b) the cumulative heat transfer rate as a function of film thickness for thin liquid films evaporating on a planar surface and a rough surface with D = 5 nm and L = 5 nm. Consistent with the results in Figure 6, the evaporating meniscus becomes flatter when only Π_{rough} is considered and steeper when only K_{rough} is considered. However, when both are considered, the evaporating meniscus becomes steeper (Figure 7a), and the cumulative heat transfer rate smaller than that on a planar surface (Figure 7b), indicating that K_{rough} has a more pronounced influence than disjoining pressure on thin film evaporation on the rough surface with D = 5 nm and L = 5 nm. This result demonstrates that surface

roughness may inhibit thin film evaporation for certain geometries, which has not been previously reported with existing thin film evaporation models or experiments.

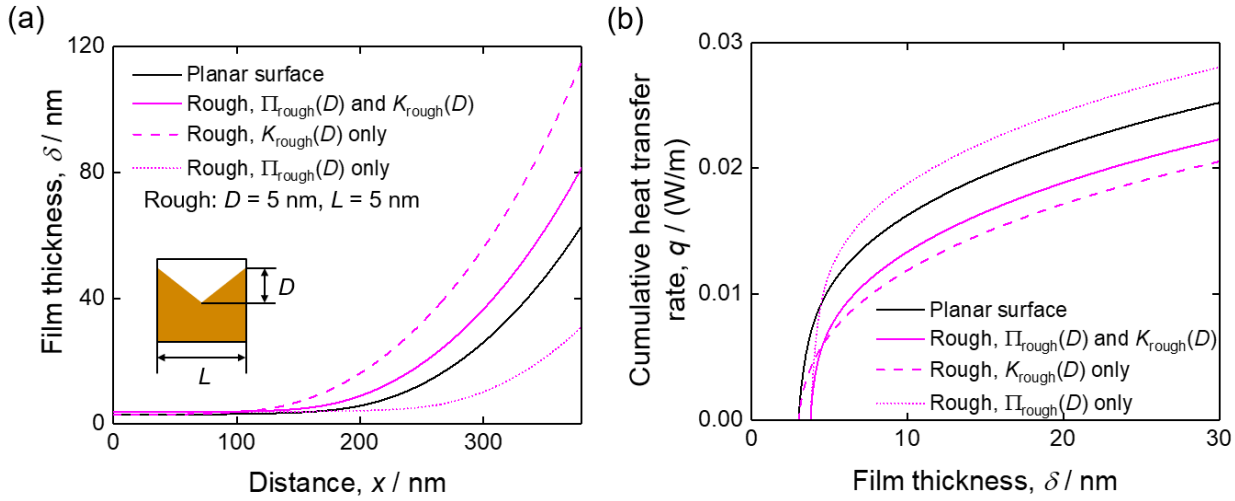

Figure 7. (a) The thickness profile and (b) the cumulative heat transfer rate as a function of film thickness for an evaporating meniscus on a planar surface and a rough surface (V-groove with D = 5 nm and L = 5 nm). The black solid lines represent the results for the planar surface. The pink solid lines represent the results for the rough surface accounting for both the roughness-affected flow permeability, K_{rough}, and the roughness-affected disjoining pressure, Π_{rough}. The pink dashed and dotted lines represent the results for the rough surface accounting for only K_{rough} and only Π_{rough}, respectively.

3.3 Parametric Study of Thin Film Evaporation on V-Grooved Surfaces

As surface roughness may enhance or inhibit thin film evaporation, depending on the specific structure characteristics, it becomes important to delimit the parameter space over which heat transfer is enhanced. To this end, a parametric study using the V-grooved surfaces summarized in Table 2 is performed to investigate the effect of the depth and the pitch on the thickness profile and the cumulative heat transfer rate of thin film evaporation.

Table 2. Summary of rough surfaces evaluated.

Depth, *D* / nm	2.5	5	7.5	5	5	5	5	5	5
Pitch, *L* / nm	20	20	20	5	10	30	100	500	10,000

Figure 8 shows (a) the thickness profile and (b) the cumulative heat transfer rate for thin liquid films evaporating on V-grooved surfaces with different depths of D = 2.5 nm, 5 nm, and 7.5 nm at a fixed pitch of L = 20 nm. A planar surface is shown for reference and can be regarded as a limiting case of a V-grooved surface with the depth, D, approaching zero. As the depth increases, the evaporating meniscus becomes flatter, leading to higher cumulative heat transfer rate. As shown in Figure 8a, the thickness profiles for different structure depths intersect at a relatively low film thickness, consistent with the experimental observations made using interferometry [6]. The intersection results from larger adsorbed film thickness induced by the increased disjoining pressure on rough surfaces with larger depths [6, 45].

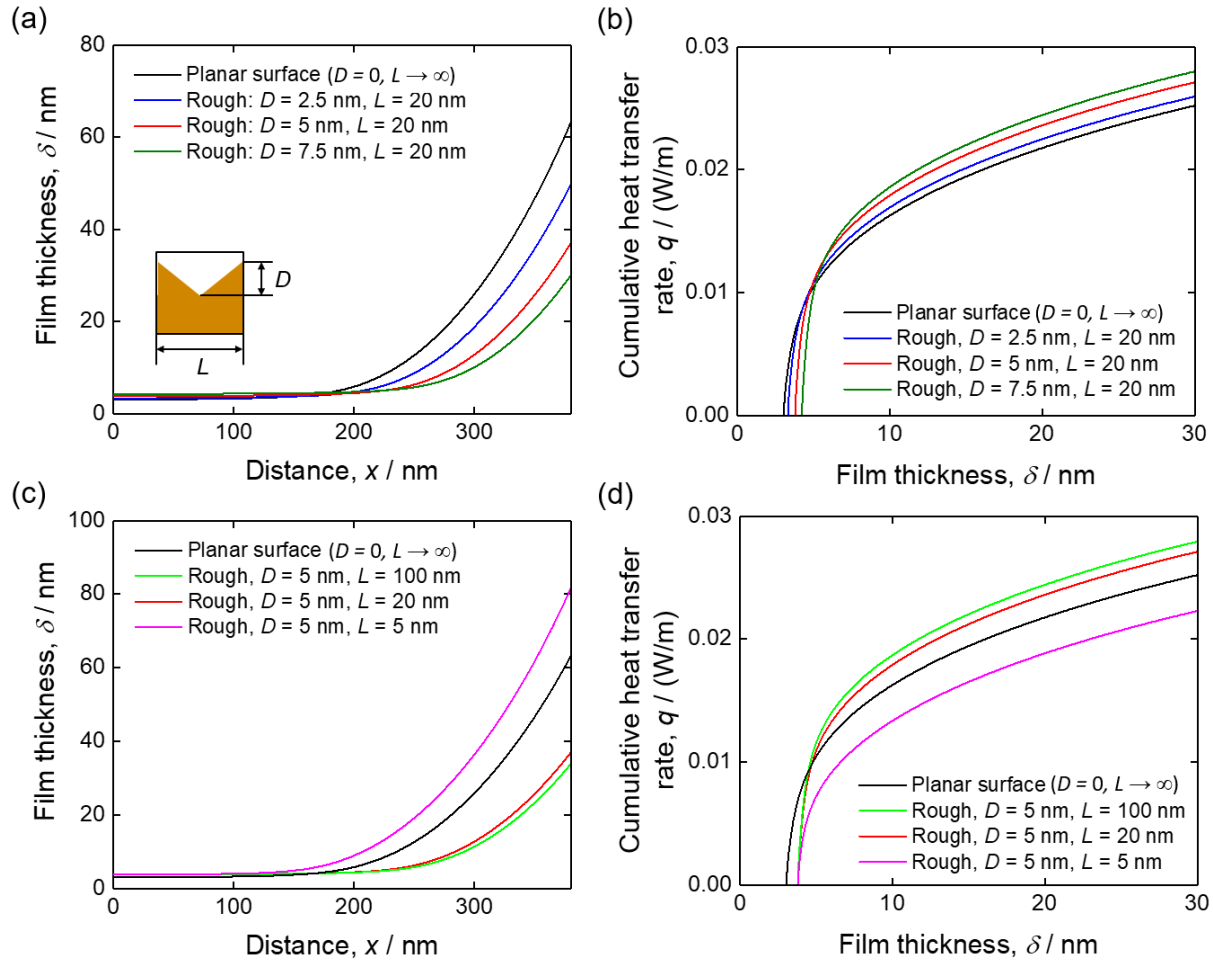

Figure 8. Effect of (a-b) the structure depth and (c-d) pitch on thin film evaporation showing (a) the thickness profile and (b) the cumulative heat transfer rate as a function of film thickness for an evaporating thin film on a planar surface and V-grooved surfaces with different depths (D = 2.5, 5, and 7.5 nm) and a fixed pitch of L = 20 nm; (c) the thickness profile and (d) the cumulative heat transfer rate as a function of film thickness for an evaporating thin film on a planar surface and V-grooves with different pitches (L = 5, 20, and 100 nm) and a fixed depth of D = 5 nm.

Figure 8 shows (c) the thickness profile and (d) the cumulative heat transfer rate as a function of film thickness for thin film evaporation on a planar surface and V-grooved surfaces with different pitches of L = 5 nm, 20 nm, and 100 nm at a fixed structure depth of D = 5 nm. The planar surface can be regarded as a V-grooved surface with the pitch, L, approaching infinity. As shown in Figure 8c and 8d, the dependence of the thickness profile and the cumulative heat transfer rate on the pitch is nonmonotonic. As the pitch is reduced from infinity (planar surface, black line) to

100 nm (green line), the evaporating meniscus becomes flatter and the cumulative heat transfer rate becomes larger. However, as the pitch is reduced from 100 nm (green line) to 20 nm (red line) and 5 nm (pink line), the evaporating meniscus becomes steeper and the cumulative heat transfer rate smaller. This nonmonotonic trend indicates that the roughness-affected disjoining pressure and flow permeability dominate over each other at different pitches.

Figure 9 plots a normalized cumulative heat transfer rate at the film thickness of $\delta = 30$ nm as a function of the depth, D, at a fixed pitch of $L = 20$ nm (Fig. 9a), and as a function of the inverse of the pitch, L^{-1}, at a fixed depth of $D = 5$ nm (Fig. 9b). The cumulative heat transfer rates at this film thickness for the rough surfaces are normalized by the rate for a planar surface. As shown in Figure 9a, the normalized cumulative heat transfer rate for rough surfaces is higher than that of a planar surface, and it increases monotonically with the depth. This observation indicates that the effect of disjoining pressure is more pronounced than flow permeability at $L = 20$ nm, and the rate increases with the depth. Based on a scaling analysis performed on the governing equation of the thickness profile, *viz.* Equation (2) (see details in the Supplemental Material), disjoining pressure is more sensitive to the depth than flow permeability in both limits of $D \to 0$ and $D \to \infty$. Therefore, the trend with depth will hold for all cases. However, there would exist a practical upper limit on the structure depth where the basic assumptions of the model (*e.g.*, the complete wetting assumption) fail.

As shown in Figure 9b, the normalized cumulative heat transfer rate increases with the inverse of the pitch at small L^{-1}, and decreases at large L^{-1}. Based on the scaling analysis, at small L^{-1} (*i.e.*, large L), the disjoining pressure is more sensitive to the variation of L^{-1} than the flow permeability. As a result, increasing L^{-1} leads to a stronger disjoining pressure and thus enhanced thin film evaporation. On the other hand, at large L^{-1} (*i.e.*, small L), the flow permeability is more sensitive to the variation of L^{-1} than the disjoining pressure; increasing L^{-1} leads to a smaller flow permeability and thus inhibits thin film evaporation. There exists an optimal pitch, L_{opt}, that leads to a maximized cumulative heat transfer rate. It is also noted that there exists a critical pitch, L_{crit}, below which the cumulative heat transfer rate of the rough surface is smaller than that of the planar surface.

The analysis performed in the present work is based on Schrage's evaporation model [36] using the material properties and operating conditions summarized in Table 1. This evaporation model

has been shown to predict the evaporation flux accurately for a broad range of parameters when the pressure difference across the liquid-vapor interface is the driving potential, but loses its accuracy for systems far from the equilibrium state [46]. Further, reported values of the accommodation coefficient span a relatively large range for some working fluids (*e.g.* water). While these factors may affect the quantitative predictions (*e.g.* the values of L_{opt} and L_{crit}), as detailed in the scaling analysis in the Supplemental Material, parameter regimes where the surface roughness improves and inhibits evaporation are demonstrated to universally exist regardless of the evaporation model applied and the material properties and operating conditions used.

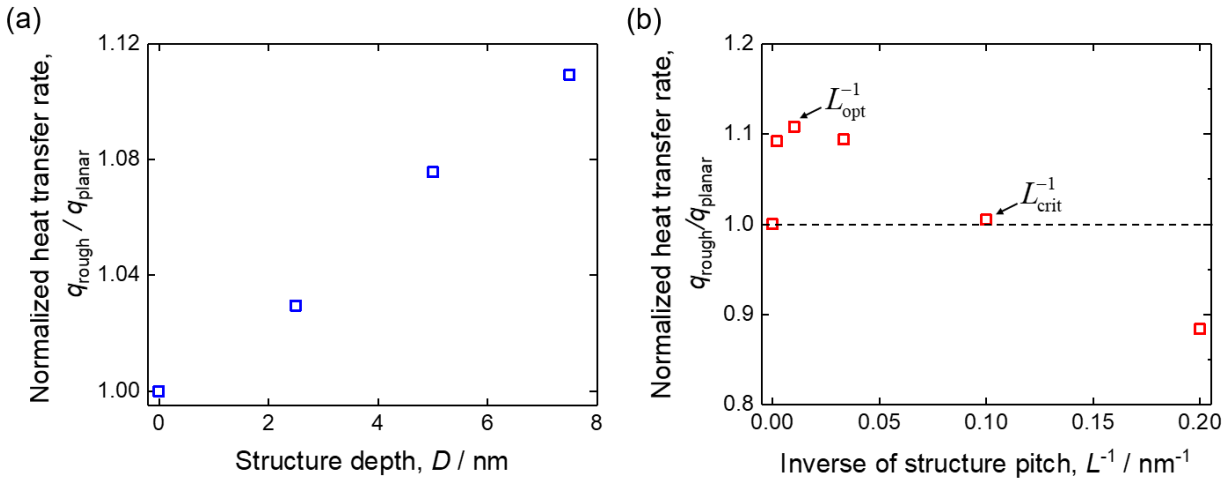

Figure 9. Normalized heat transfer rate at the film thickness of 30 nm as a function of (a) the structure depth and (b) the inverse of the structure pitch for thin film evaporation on V-grooved surfaces.

4. Conclusions

In this study, a theoretical model is derived for thin film evaporation on rough surfaces. The roughness-affected disjoining pressure is predicted based on the Derjaguin approximation and validated against a direct integration of solid-liquid potential. The model developed here for disjoining pressure on rough surfaces offers a more accurate description than using an effective Hamaker constant. The roughness-affected flow permeability is determined by balancing the driving pressure versus the viscous resistance. These roughness-affected factors are coupled to the thin film evaporation model to account for the influence of the surface structures. The present work identifies the competing roles of the roughness-affected disjoining pressure and the roughness-

affected flow permeability during thin film evaporation and reveals a regime of the parameter space where surface structures inhibit thin film evaporation. The model predicts that surface structures lead to enhanced thin film evaporation when the effect of disjoining pressure is more pronounced, consistent with existing experiments. However, the model reveals that surface structures may inhibit thin film evaporation when the effect of flow permeability is more pronounced. This result calls for experimental studies to confirm the inhibition effect of surface structures on thin film evaporation. A parametric study is performed to investigate the effect of the structure depth and pitch on thin film evaporation. The results show that the cumulative heat transfer rate increases monotonically with the structure depth. Furthermore, there exists an optimal pitch for rough surface structures where the cumulative heat transfer rate is maximized. When the pitch is further reduced to a critical value, the surface roughness may inhibit thin film evaporation. The model developed in this work can guide the design of roughness structures for improving two-phase heat transfer.

Acknowledgments

This work was supported in part by Purdue's NEPTUNE Center for Power and Energy, funded by the Office of Naval Research under Grant No. N000141613109. This work used the Extreme Science and Engineering Discovery Environment (XSEDE), which is supported by National Science Foundation grant number ACI-1548562.

Appendix A. Supplementary material

Supplementary material associated with this article can be found in the online version.

References

[1] J. Plawsky, A. Fedorov, S.V. Garimella, H. Ma, S. Maroo, L. Chen, Y. Nam, Nano-and microstructures for thin-film evaporation—A review, Nanosc Microsc Therm, 18(3) (2014) 251-269.

[2] O. Mahian, A. Kianifar, S.Z. Heris, D. Wen, A.Z. Sahin, S. Wongwises, Nanofluids effects on the evaporation rate in a solar still equipped with a heat exchanger, Nano Energy, 36 (2017) 134-155.

[3] S.P. Fisenko, A.A. Brin, A.I. Petruchik, Evaporative cooling of water in a mechanical draft cooling tower, Int. J. Heat Mass Transfer, 47(1) (2004) 165-177.

[4] F. Su, N. Zhao, Y. Deng, H. Ma, An ultrafast vitrification method for cell cryopreservation, J. Heat Transfer, 140(1) (2017) 012001.

[5] H. Wang, S.V. Garimella, J.Y. Murthy, Characteristics of an evaporating thin film in a microchannel, Int. J. Heat Mass Transfer, 50(19-20) (2007) 3933-3942.

[6] M. Ojha, A. Chatterjee, G. Dalakos, P.C. Wayner, Jr., J.L. Plawsky, Role of solid surface structure on evaporative phase change from a completely wetting corner meniscus, Phys. Fluids, 22(5) (2010) 052101.

[7] B. Bon, J.F. Klausner, E. Mckenna, The Hoodoo: A new surface structure for enhanced boiling heat transfer, J. Therm. Sci. Eng. Appl., 5(1) (2013) 011003.

[8] H.J. Cho, D.J. Preston, Y. Zhu, E.N. Wang, Nanoengineered materials for liquid–vapour phase-change heat transfer, Nat. Rev. Mater., 2(2) (2017) 16092.

[9] C. Li, G. Peterson, Y. Wang, Evaporation/boiling in thin capillary wicks (l)—wick thickness effects, J. Heat Transfer, 128(12) (2006) 1312-1319.

[10] S. Sarangi, J.A. Weibel, S.V. Garimella, Quantitative evaluation of the dependence of pool boiling heat transfer enhancement on sintered particle coating characteristics, J. Heat Transfer, 139(2) (2016) 021502.

[11] M.M. Rahman, E. Ölçeroğlu, M. McCarthy, Role of wickability on the critical heat flux of structured superhydrophilic surfaces, Langmuir, 30(37) (2014) 11225−11234.

[12] D.S. Antao, S. Adera, Y. Zhu, E. Farias, R. Raj, E.N. Wang, Dynamic evolution of the evaporating liquid–vapor interface in micropillar arrays, Langmuir, 32(2) (2016) 519-526.

[13] S. DasGupta, J.L. Plawsky, P.C. Wayner, Interfacial force field characterization in a constrained vapor bubble thermosyphon, AlChE J., 41(9) (1995) 2140-2149.

[14] M.S. Hanchak, M.D. Vangsness, L.W. Byrd, J.S. Ervin, Thin film evaporation of n-octane on silicon: Experiments and theory, Int. J. Heat Mass Transfer, 75 (2014) 196-206.

[15] M. Potash Jr, P.C. Wayner Jr, Evaporation from a two-dimensional extended meniscus, Int. J. Heat Mass Transfer, 15(10) (1972) 1851-1863.

[16] K. Park, K.-J. Noh, K.-S. Lee, Transport phenomena in the thin-film region of a micro-channel, Int. J. Heat Mass Transfer, 46(13) (2003) 2381-2388.

[17] S. Narayanan, A.G. Fedorov, Y.K. Joshi, Interfacial transport of evaporating water confined in nanopores, Langmuir, 27(17) (2011) 10666-10676.

[18] H. Wang, S.V. Garimella, J.Y. Murthy, An analytical solution for the total heat transfer in the thin-film region of an evaporating meniscus, Int. J. Heat Mass Transfer, 51(25–26) (2008) 6317-6322.

[19] C. Yan, H.B. Ma, Analytical solutions of heat transfer and film thickness in thin-film evaporation, J. Heat Transfer, 135(3) (2013) 031501.

[20] R. Ranjan, J.Y. Murthy, S.V. Garimella, A microscale model for thin-film evaporation in capillary wick structures, Int. J. Heat Mass Transfer, 54(1-3) (2011) 169-179.

[21] V.S. Ajaev, T. Gambaryan-Roisman, P. Stephan, Static and dynamic contact angles of evaporating liquids on heated surfaces, J. Colloid Interface Sci., 342(2) (2010) 550-558.

[22] V.S. Ajaev, O.A. Kabov, Heat and mass transfer near contact lines on heated surfaces, Int. J. Heat Mass Transfer, 108 (2017) 918-932.

[23] S. Batzdorf, T. Gambaryan-Roisman, P. Stephan, Direct numerical simulation of the microscale fluid flow and heat transfer in the three-phase contact line region during evaporation, J. Heat Transfer, 140(3) (2017) 032401-032401-032410.

[24] S. Herbert, S. Fischer, T. Gambaryan-Roisman, P. Stephan, Local heat transfer and phase change phenomena during single drop impingement on a hot surface, Int. J. Heat Mass Transfer, 61 (2013) 605-614.

[25] H.C. Hamaker, The London—van der Waals attraction between spherical particles, Physica, 4(10) (1937) 1058-1072.

[26] I.E. Dzyaloshinskii, E.M. Lifshitz, L.P. Pitaevskii, The general theory of van der Waals forces, Adv. Phys., 10(38) (1961) 165-209.

[27] V. Panella, R. Chiarello, J. Krim, Adequacy of the Lifshitz theory for certain thin adsorbed films, Phys. Rev. Lett., 76(19) (1996) 3606-3609.

[28] D. Beaglehole, E.Z. Radlinska, B.W. Ninham, H.K. Christenson, Inadequacy of Lifshitz theory for thin liquid-films, Phys. Rev. Lett., 66(16) (1991) 2084-2087.

[29] B.V. Derjaguin, N.V. Churaev, Structural component of disjoining pressure, J. Colloid Interface Sci., 49(2) (1974) 249-255.

[30] A. Sharma, A.T. Jameel, Nonlinear stability, rupture, and morphological phase separation of thin fluid films on apolar and polar substrates, J. Colloid Interface Sci., 161(1) (1993) 190-208.

[31] H. Wong, S. Morris, C.J. Radke, Three-dimensional menisci in polygonal capillaries, J. Colloid Interface Sci., 148(2) (1992) 317-336.

[32] M.C. Thomas, S.P. Beaudoin, An enhanced centrifuge-based approach to powder characterization: Experimental and theoretical determination of a size-dependent effective Hamaker constant distribution, Powder Technol., 306 (2017) 96-102.

[33] M.O. Robbins, D. Andelman, J.-F. Joanny, Thin liquid films on rough or heterogeneous solids, Phys. Rev. A, 43(8) (1991) 4344-4354.

[34] H. Hu, C.R. Weinberger, Y. Sun, Effect of nanostructures on the meniscus shape and disjoining pressure of ultrathin liquid film, Nano Lett., 14(12) (2014) 7131-7137.

[35] M.R. Stukan, P. Ligneul, J.P. Crawshaw, E.S. Boek, Spontaneous imbibition in nanopores of different roughness and wettability, Langmuir, 26(16) (2010) 13342-13352.

[36] R.W. Schrage, A theoretical study of interphase mass transfer, Columbia University Press, 1953.

[37] A. Faghri, Heat pipe science and technology, Taylor & Francis, 1995.

[38] B. V. Derjaguin, N. V. Churaev, V.M. Muller, Surface forces, Consultants Bereau, New York, 1987.

[39] B.A. Todd, S.J. Eppell, Probing the limits of the Derjaguin approximation with scanning force microscopy, Langmuir, 20(12) (2004) 4892-4897.

[40] H. Hu, C.R. Weinberger, Y. Sun, Model of meniscus shape and disjoining pressure of thin liquid films on nanostructured surfaces with electrostatic interactions, J. Phys. Chem. C, 119(21) (2015) 11777-11785.

[41] H. Hu, M. Chakraborty, T.P. Allred, J.A. Weibel, S.V. Garimella, Multiscale modeling of the three-dimensional meniscus shape of a wetting liquid film on micro-/nanostructured surfaces, Langmuir, 33(43) (2017) 12028-12037.

[42] Z. Lu, I. Kinefuchi, K.L. Wilke, G. Vaartstra1, E.N. Wang, A unified relationship for evaporation kinetics at low Mach numbers, Nat. Commun., 10 (2019) 2368.

[43] B.A. Grigoryev, B.V. Nemzer, D.S. Kurumov, J.V. Sengers, Surface tension of normal pentane, hexane, heptane, and octane, Int. J. Thermophys., 13(3) (1992) 453-464.

[44] K.R. Harris, R. Malhotra, L.A. Woolf, Temperature and density dependence of the viscosity of octane and toluene, J. Chem. Eng. Data, 42(6) (1997) 1254-1260.

[45] H. Hu, Y. Sun, Effect of nanostructures on heat transfer coefficient of an evaporating meniscus, Int. J. Heat Mass Transfer, 101 (2016) 878-885.

[46] H. Wang, From contact line structures to wetting dynamics, Langmuir, 35 (2019), 10233-10245.

Graphical Abstract: